Low Temperature Synthesis and Spark Plasma Sintering of a Boron Carbide with a Low Residual Carbon Content

Jonathan Kenny[a], Nikkia McDonald[a], Jon Binner[a], Isaac Tsz Hong Chang[b], Sylvain Marinel[c]

[a] Materials and Metallurgy Department, Elms Road, The University of Birmingham, Edgbaston, West Midlands, England, B15 2TT, j.binner@bham.ac.uk

[b] LiME Training Centre, Brunel University London, Kingston Lane, Uxbridge, Middlesex, England, UB8 3PH, Isaac.chang@brunel.ac.uk

[c] CNRT 6, Boulevard Maréchal Juin, CEDEX 4, Caen, 14050, France, sylvain.marinel@ensicaen.fr

Abstract

Using spark plasma sintering (SPS), >98.5 % dense boron carbide (B_4C) samples were made from commercially available and lab-synthesised powders, the latter made via a low temperature synthesis (LTS) process. The work showed that the LTS powder can be produced in batches of tens to hundreds of grams whilst maintaining a high purity material with lower levels of residual free carbon (20.6 – 21.3 wt.% C) than commercially available samples (22.4 wt.% C). This is thought to allow the former material to exhibit higher hardness values (37.8 GPa) than the latter (32.5 GPa) despite featuring a coarser average grain size (10.8 μm and 2.4 μm respectively).

Keywords: Boron carbide, low temperature synthesis, spark plasma sintering (SPS).

1. Introduction

There is a great need in the defence sector for the development of hard, lightweight ceramics for use in protection against a range of small arms fire ballistic threats with different kinetic energies [1,2]. Whilst ceramics such as alumina (Al_2O_3) and silicon carbide (SiC) have demonstrated adequate resistance, B_4C offers lower densities and higher hardness values, theoretically making it a suitable material. Unfortunately, it experiences shock-induced amorphisation, otherwise known as *'shatter gap'*, which causes the B_4C unit cell to collapse from rhombohedral to amorphous, deteriorating the materials' ballistic performance due to exacerbated crack propagation [3,4].

Various methods have been investigated to prevent amorphisation within the material, including reducing the materials' grain size down to the nanoscale to limit the strain accommodated per grain [5] and doping the crystal structure to substitute atoms within the unit cells' inter-icosahedral chains. The latter makes them more susceptible to plastic deformation and reduces amorphisation [6,7]. Similar results have also been achieved by moving to boron, B, rich stoichiometries [8,9]. This approach has the additional benefit of reducing the materials' residual carbon, C, content, which usually migrates, nucleates and grows within the microstructure during sintering to form undesirable graphitic precipitates [10–13].

There has been much work focused on the production of low-carbon B_4C. Mondal & Banthia [14] and Hadian & Bigdeloo [15] have approached this via the pyrolysis of a sol gel-like polyvinylborane (PVB). This process forms an intimate mixture of boron oxide, B_2O_3, and carbon that are reacted together via carbothermal reduction (CR) to form B_4C via the LTS method. This involves reacting the precursors together over several hours at temperatures below 1500 ^oC. The main advantages of this method are that it is less energy intensive to carry out and can be done using readily commercially available equipment. However, it faces a significant disadvantage insofar as the precursors agglomerate together when processed in large quantities and therefore require considerable grinding after being reacted; given the high hardness of B_4C this results in samples with high impurity levels [14-15].

Weimer et al. [16] and Toksoy et al. [17] have achieved the same goal through the use of rapid carbothermal reduction, RCR. This involved passing a similar pyrolysed precursor with a B-rich composition down a high temperature furnace tube at well above 1500 ^oC to form the ceramic within seconds to minutes. The approach, however, requires tailor made equipment and is not easily commercialised.

Other routes have also been investigated to consolidate these powders, often involving hot isostatic pressing. Whilst this yields components with a higher and more uniform density compared to uniaxial pressing followed by conventional sintering, it requires relatively long sintering times [18]. Spark plasma sintering (SPS) has also been investigated, which makes use of rapid Joule heating to bypass grain growth mechanisms whilst facilitating densification [19].

To date, the only SPS studies that have been undertaken with low carbon content B_4C have involved powders made by the RCR method. Hence the purpose of this work was to manufacture low carbon B_4C via the LTS method using readily available and processable precursor materials and consolidate them together via SPS. Chemical and mechanical characterisation were performed on the powders and green bodies, as well as after sintering, and the results were compared with samples made from commercially sourced B_4C powder.

2. Experimental

2.1. Sample Preparation

Boric acid, H_3BO_3, reacts with C via the following overall reaction, which consists of two stages, H_3BO_3 thermally decomposing to B_2O_3 at 150 ^oC, which then reacts with C at temperatures exceeding ~1200 ^oC [20]:

$$4H_3BO_3 \rightarrow 2B_2O_3 + 6H_2O \quad \textit{(1a)}$$

$$2B_2O_3 + 7C \rightarrow B_4C + 6CO \quad \textit{(1b)}$$

H_3BO_3 (≥99.5 % pure electrophoresis grade, Merck Life Science UK Ltd, Gillingham, UK) and modified waxy maize starch powders (<85 mesh size, 100 % pure, Univar via TasteTech Ltd, Bristol, UK) were dissolved in de-ionised (DI) water at 85 ^oC in a mass ratio of 1.15 : 1 H_3BO_3 : modified starch. The use of excess H_3BO_3 followed the work of Gao [21] who quantified the level of volatilisation that occurred. The solution was diluted by the further addition of DI water in a mass ratio of 1:30 before being stirred for 2 h at 750-1000 rpm until a clear solution was obtained. This was spray dried in 10 kg batches (Drytec Spray Drying Ltd, Tonbridge, UK) using an inlet temperature of 190 ^oC, outlet temperature of 90 ^oC and a nozzle pressure of 5 bar.

The spray-dried precursor was subjected to a 3-stage heat treatment, fig. 1. The first stage involved drying 500 g batches at 125 ^oC for 64 h in a box furnace (CWF1100, Carbolite-Gero Ltd., Hope, UK) to remove any physiosorbed water from the spray-dried particles. Half-way through the drying process, the powder was manually stirred to ensure the powders dried homogeneously. Following light deagglomeration by milling at 49 rpm for 10 mins in 1 l high-density polyethylene (HDPE) bottles with 14 mm diameter stainless steel ball bearings (T2F turbula shaker-mixer, Gell-Mills Ltd., Clifton, NJ, USA) the powder was poured through a ~1.6 mm mesh to remove the ball bearings, whilst any retained agglomerates were crushed manually. A custom made induction furnace (Scanwel Ltd., Bala, UK) was then used to pyrolyse the powders in graphite crucibles in 150 g batches. After sealing, the furnace chamber was evacuated to 0.6 MPa and flushed twice with Ar before heating began. During pyrolysis at 650 ^oC for 2 h, Ar was flowed through the powder at 5 l/min via an Ar lance, fig. 1. The heating and cooling rates were ~125 ^oC/min and ~5 ^oC/min respectively. At the end of the pyrolysis, the powders were de-agglomerated using the same sieve as described above.

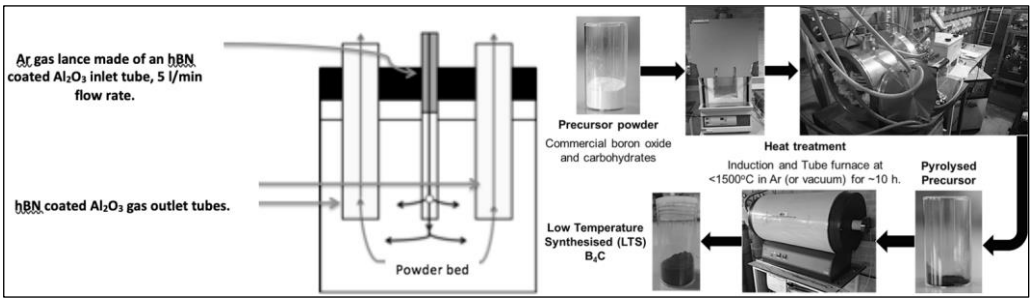

Figure 1: *3-stage heat treatment and pyrolysis process for low carbon B_4C*

Carbothermal reduction was achieved in a tube furnace (TSH16/75/610-2416CG, Elite Thermal Systems Ltd., Market Harborough, UK), the pyrolysed powders being loaded into 5 graphite crucibles each containing ~20 g of powder. The reaction occurred at 1450 ^{o}C for 5 h under a 5 l/min laminar flow of Ar with a heating and cooling rate of 10 ^{o}C/min. The powders were milled for 15 mins in an XRD microniser mill (McCrone Group, Westmont, IL, USA)[1] in 10 g batches with 50 zirconia-toughened alumina (ZTA) beads. The powders were then sieved using a 500 μm mesh to separate them from the beads and any large agglomerates.

Densification was undertaken using an SPS (HPD 25/2, FCT Systeme GmbH; Rauenstein, Germany) at the facility in CNRT, France, with 2.5 g batches of powder being sintered. Half of the sintered samples were synthesised from the low carbon B_4C powder produced in this work whilst the other half were made from HS grade boron carbide powder (H.C. Starck GmbH, Karlsruhe, Germany, d_{50} = 1 μm). According to the manufacturer, this grade contains 22.6 wt.% bound and free carbon, as well as <1 to <0.01 wt.% of other impurity elements; in descending order of abundance O, N, Si, Fe and Al.

A 3-stage heat treatment process under a vacuum of <100 Pa was used for all samples. The first stage involved heating from 400 to 1300 ^{o}C at 100 ^{o}C/min whilst simultaneously increasing the pressure from 28 to 45 MPa; the samples were then held for 5 mins. This ensured any B_2O_3 on the B_4C grain boundaries sublimed, thereby enhancing the materials' sinterability [22]. The second stage saw the temperature increased to 1900 ^{o}C, also at 100 ^{o}C/min, and when the peak temperature was reached, the pressure was increased from 45 to 80 MPa over a 5 min period before the samples were held for 40 mins. After densification, the samples were cooled to 400 ^{o}C at 50 ^{o}C/min. Hexagonal boron nitride (hBN, Kennametal Ltd., Newport, UK) was used as a solid lubricant to retrieve the samples. After each sintering run, the samples and die pieces were thoroughly cleaned to avoid the contamination of other samples with residual hBN.

The graphite paper used to line the dies always fused to the surfaces of the samples; it was removed using a P80 diamond-plated disk. When required, some samples were cross sectioned using either an Accutom-5 or 50 saw with a small-radius diamond tipped disc blade spinning at 3000 rpm. Due to the brittle nature of the material, samples needed to be embedded in Versocit or Epofix resin and were sliced at a feed-rate of only 5 μm/s. Grinding and polishing involved the use of a P120 polishing wheel and diamond-particle suspensions of decreasing size, from 9, 6, 3 to 1 μm, followed by an activated silica (OPS) suspension. Each stage took about 10 mins and all samples were cleaned between stages to minimise contamination. All the equipment in this stage was supplied by Struers Ltd. (Rotherham, UK).

[1] Undertaken in the Department of Materials at Loughborough University.

Chemical etching involved submerging the samples in 1% of aqueous KOH solution (diluted from 45 % solution with DI water, Merck Life Science UK Ltd.) whilst attached to a power pack (EP-603, Manson Engineering Ltd., Kwai Chung, Hong Kong) set to deliver 1 V and 0.3 A. The anode was attached to a copper O-ring at the bottom of the beaker and the cathode to the sample via a crocodile clip. Etching was done for 80 s before being washed with ethanol, although some samples required 90 s before the microstructure was visible.

2.2. Characterisation

X-ray diffraction was used for phase analysis of the powders, green and sintered samples (XPert Pro X-ray diffraction unit, Malvern Panalytical Ltd., Malvern, UK)[2] over 15 – 90° 2θ using Cukα radiation at a scan rate of 0.3125 °/min. Rietveld refinement based Phase Quantative Analysis (PQA) was used to determine the chemical stoichiometry of the B_4C in each sample. TOPAS software (Coelho Software Ltd., Brisbane, Australia), in conjunction with appropriate JEdit scripts (www.jedit.org), was used to reference the data from each refinement to published crystallographic data [23]

An Invia Raman spectrometer (Renishaw plc., Wotton-Under-Edge, UK) was used to analyse the powder and the sintered samples, the latter on internal surfaces cut parallel and perpendicular to the pressing axis and external surfaces. A 100x objective was used with a 10 mW red 633 nm He-Ne laser and a diffraction grating with 1200 lines/mm. At least 3 regions were analysed per sample using a laser spot size diameter of <1 μm. All of the bulk ceramic samples were analysed at the maximum laser power (50-100 %) to provide a high signal: background ratio; the laser exposure time was 60 s and 10 measurements were made for each analysed region.

To obtain micrographs of the analysed materials, as well as to investigate how corner cracks interacted with the grain boundaries of the sintered samples, an XL-30 Environmental SEM (ESEM – ThermoFisher Scientific Ltd.; Hillsboro, OR, USA) was used to analyse the samples under 200x, 1,000x, 2,000x, 5,000x and 10,000x magnifications. As the analysed samples were also made up of light elements, a spot size of 3 and an acceleration voltage of 10 kV were used, in conjunction with gold coatings deposited by an Emscope SC500 sputtering machine (Quorum Technologies Ltd.; Laughton, UK). Additional fracture surface images were collected using an FEI Quanta 600F (ThermoFisher Scientific Ltd.) with an INCAx-sight Energy Dispersive X-Ray Spectroscopy (EDS) detector[3] (Oxford Instruments NanoAnalysis & Asylum Research Ltd.; High Wycombe, UK). The SEM was used in low vacuum mode under a 20 kV acceleration voltage. A JEM-2100 TEM (Jeol USA Inc., Peabody, MA, USA) was used to analyse dried powder and suspension samples, which were drop cast onto 300 mesh formvar backed copper grids.

[2] Undertaken in ENSICAEN, Caen, France.
[3] This work was carried out at the Department of Chemistry at the University of Reading.

An R-Series Laser Scattering Particle Size (LSPS) analysis machine (Sympatec GmbH; Clausthal-Zellerfeld, Germany) with a 5 mW He-Ne laser (632.8 nm wavelength) was used to obtain particle size distributions of the powders. Dilute suspensions of the powders were prepared by adding a few milligrams of powder to 5 ml glass vials using 0.1 M sodium pyrophosphate tetrabasic ($Na_4P_2O_7$, ≥99.5 % pure – Merck Life Science UK Ltd.) surfactant and then filling the rest of the vial with deionised water and shaking manually to homogenise the suspension.

To investigate mass loss and heat flow as a function of temperature in each of the tested raw materials, a STA449C heat flux TGA/DSC unit was used in conjunction with a TASC 414/3A heat controller and 414/4 thermal analysis units (Netzsch-Gerätebau GmbH; Wolverhampton, UK). Each sample was heated from room temperature to 1600 ^oC under an atmosphere of flowing Ar and with a heating rate of 10 ^oC/min. All tested samples were loaded in 10 mg batches into an Al_2O_3 DSC pan (Perkin Elmer Ltd., Seer Green, UK), which was placed in one chamber, whilst an empty pan was placed into a control chamber.

The total C content of the powders was determined using an EA1110 elemental analyser (CE Instruments Ltd., Wigan, UK). Samples were held at -110 ^oC for approximately 1 week prior to testing (Scanvac Coolsafe freeze drier, LaboGene ApS; Lillerød, Denmark) to ensure that any atoms from physiosorbed H_2O molecules on the surface of the B_4C particles would have a minimal effect on the readings obtained. The densities of the sintered samples were obtained via the Archimedes method and using alcohol (absolute grade, 99 % Pure, Thermofisher Scientific Ltd.).

Topographical images from the surfaces of the sintered samples were collected at 200x and 1,600x magnification using a Leitz Laborlux 12HL light microscope (LM - Leica Microsystems Ltd.; Milton Keynes, UK), mounted with an AxioCam ICc1 camera (Carl Zeiss Ltd.; Cambridge, UK). These images were collected on the cross sectional and cut faces of the samples. The SEM micrographs were subjected to two different grain size analysis techniques, viz. the standard 4-point linear intercept method and Image-J analysis (https://imagej.net), with calculations factoring in that the grains were of spherical and Feret's geometry [24].

A MVK-H1 Vickers micro-indentation machine (Mituyoto Ltd.; Coventry, UK) was used to determine both the hardness (H_v, GPa) and crack propagation resistance (CPR, MPa $m^{0.5}$) values of the sintered samples on their cross section surfaces. All indents were placed using a 9.81 N loading force and a 10 s dwell time. A minimum of 10 crack propagation resistance readings were taken when calculating the property value averages from the corners of the indents in each sample.

The Crack Propagation Resistance (CPR) was determined using the equation of Anstis et al. [25], viz.:

$$K_C = \delta \left(\frac{E}{H_v}\right)^{0.5} \frac{P}{c^{3/2}} \quad \textbf{(2)}$$

Where 'δ' is a constant based on the indenters geometry (~0.016 for H_v indents), 'E' is the materials Young's Modulus (GPa), 'H_v' is the materials Vickers hardness, 'P' is the indentation loading force (N) and 'c' is the distance from the indents' centre to the end of the radial crack propagating from one of its corners (m).

Nanoindentation testing (Nanotest Vantage, Micro Materials Ltd., Wrexham, UK) was used to obtain the mean Young's Modulus for 1 sample of each composition. A loading force of 10 mN was used over at least 3 points in order to calculate the average value.

3. Results and Discussion

3.1. Powder Characterisation

Fig. 2 shows the particle size distribution for the commercial grade and LTS B_4C powders. An additional 2 distributions are also present for the latter powder, which was left to settle for approximately 10 – 15 mins until a sediment and supernatant layer formed in suspension prior to testing. The distribution for the HS material was smaller on average than that of the LTS powder; varying from the submicron region to over 10 μm and with a D_{50} value above 2 μm.

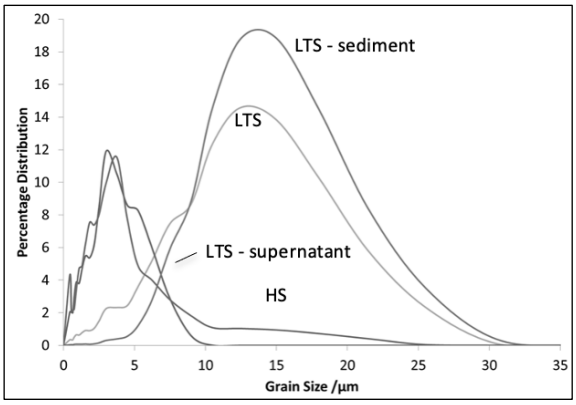

Figure 2: *Particle size distributions for the HS and LTS B_4C powders (as-mixed, supernatant and sediment layers of the settled suspension)*

When analysing the LTS powders that were shaken before testing, the average distribution was wider, ranging from 0-30 μm with a D_{50} value of roughly 12 μm. However, when left to settle, a bimodal size distribution could be observed between the particles in the settled and supernatant layers of the LTS suspension. Those in the former layer, thought to be agglomerates, had a D_{50} value of ~14 μm with a size distribution between 2 – 32.5 μm, whereas those in the latter, thought to be primary particles, had a size distribution between 0.2 – 10 μm and a D_{50} value of ~3 μm.

Fig. 3 shows SEM images for the commercial grade and LTS B_4C powders. The commercial powder particles have an approximately equiaxed, though rough, appearance that results from the grinding stages used in production. The grain size distribution of 1 – ~3 µm matches the suppliers' specification of 0.8 µm on average quite closely.

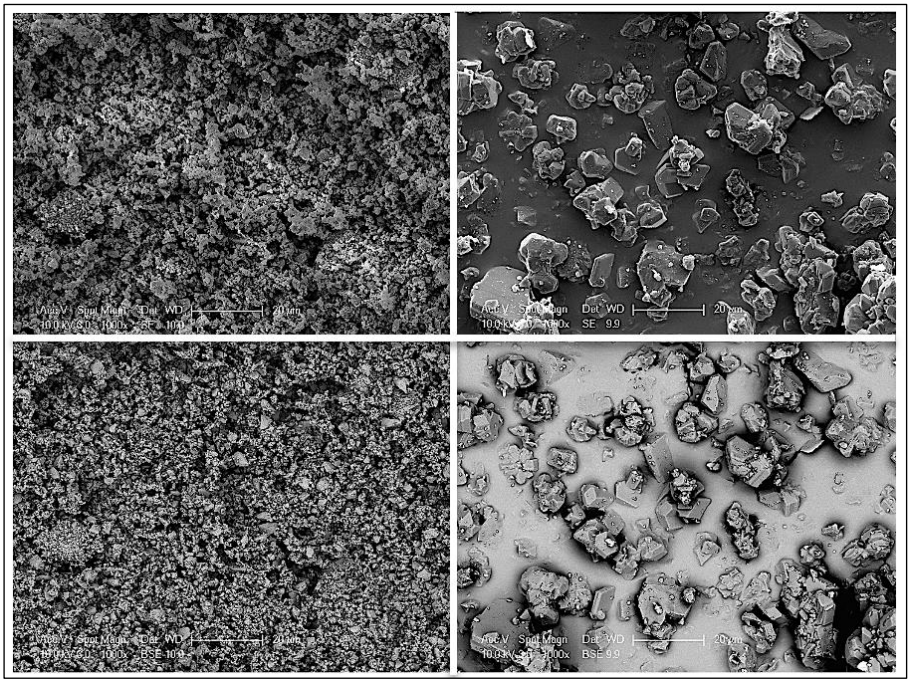

Figure 3: *200x SE micrographs of as-received HS (Left) and as-micronised LTS B_4C (right); top: SE imaging; bottom: BSE imaging, 20 µm scale bar*

Fig. 4 shows the Raman spectra for the LTS boron carbide samples compared to the HS grade sample. It primarily shows that the 2 materials share similar vibrational modal peaks – namely those that correspond to the B_4C boron carbide polytype.

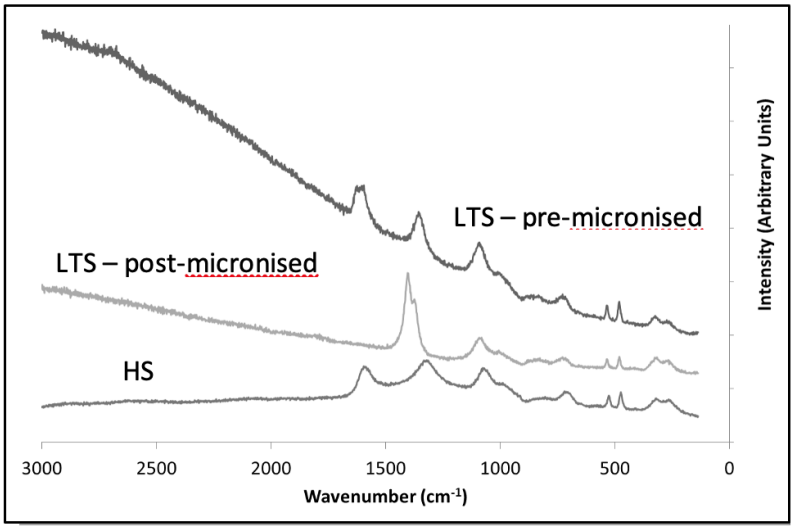

Figure 4: *Raman spectra of HS and LTS B_4C powders (0 – 3000 cm^{-1}, 633 nm laser, 100x objective)*

One area where a more considerable difference can be seen is in the C peak positions in the LTS B_4C. Whereas the G peak is indicated by a unimodal peak between 1585 – 1592 cm^{-1} in the HS grade material, the peak appears bimodal in the LTS material, with one appearing at 1601 cm^{-1} and the latter at 1629 cm^{-1} before the micronising process. This could pertain to residual C or amorphisation of the HS B_4C, which is likely to be greater than in the LTS material due to the milling and jaw crushing processes used in its production. After the LTS material is micronised, new spectral features appear in the form of a pair of bimodal peaks centred at 1373 cm^{-1} and 1405 cm^{-1}, which could be due to amorphisation from the process [26–30].

Table 1, as well as fig. 5, list the various phase changes and mass loss values that occur over the course of the DSC heating regime of the LTS B_4C precursor powder. These findings corroborate those of Liu et al. [31], who also reported that the evaporation of physiosorbed water took place well above 100 ^oC. Above 150 ^oC, the 2-stage thermal decomposition of H_3BO_3 to H_2O and B_2O_3 was observed [20].

Table 1: *DSC and mass losses of as-received LTS B_4C precursor from 22 – 1600 ^oC at 10 ^oC min^{-1} under flowing Ar*

Process	Stage	Onset temp / ^oC	End temp / ^oC	Mass loss / wt. %	Cumulative mass loss / wt. %	Endo/exo-thermic	Mass loss after process / wt. %
Drying	A	22	112	3.8	3.8	Endothermic	37.2
	B	112	194	22.3	26.1		
	C	194	300	11.1	37.2		
Pyrolysis	D	330	392	9.1	46.3	Exothermic	21.9
	E	392	1205	12.8	59.1	Endothermic	30.0
CR	F	1205	1415	26.5	85.5		
	G	1415	1600	3.5	89.1		

This study also supported Liu et al. [31] in demonstrating that the pyrolysis temperatures of complex carbohydrate precursors varied between 300 – 334 ^oC. FTIR spectroscopy, as well as XRD analysis, was also used to show that the hydrolysis of α-1,4 and α-1,6 glucosidic linkages of amylose and amylopectin molecules took place at these temperatures. This was followed by carbothermal above ~1200 ^oC, as shown by other authors [32–35].

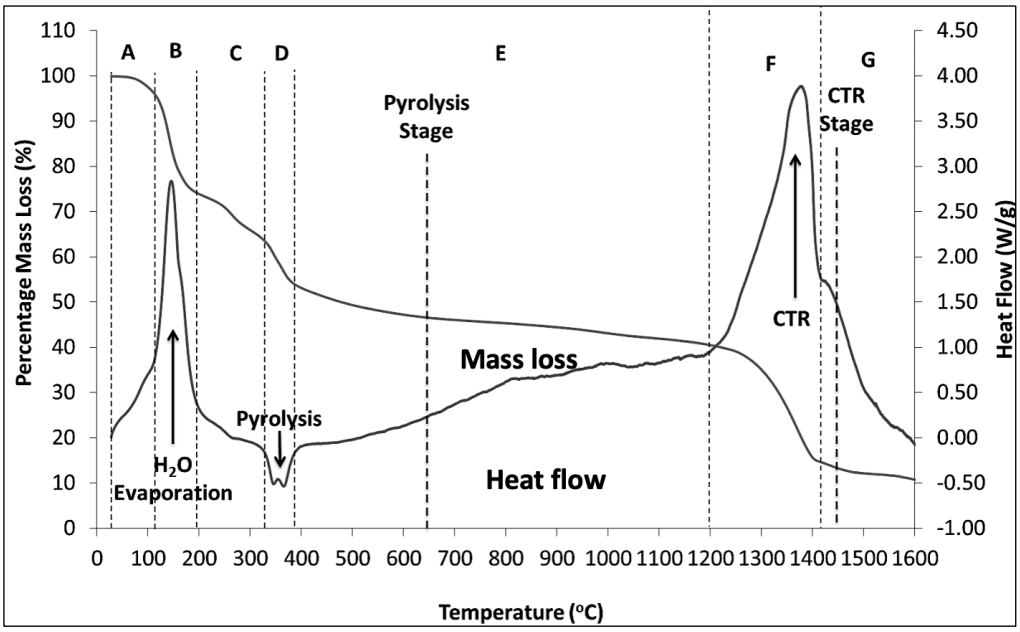

Figure 5: *Heat flow and mass loss over temperature for as-received LTS B_4C precursor from 22 – 1600 °C at 10 °C min^{-1} under flowing Ar*

3.2. Sintered Sample Characterisation

3.2.1. Microstructural Analysis

The unetched, post-sintered pressed face micrographs of the HS and LTS-based B_4C samples can be seen in fig 6. As can be seen, all of the samples feature black spheroidal regions within a bright matrix phase. The former regions are thought to be carbonaceous inclusions that form due to the migration of free C through the material's microstructure during sintering. This is corroborated by previous analyses on B_4C consolidated under similar conditions [10–13].

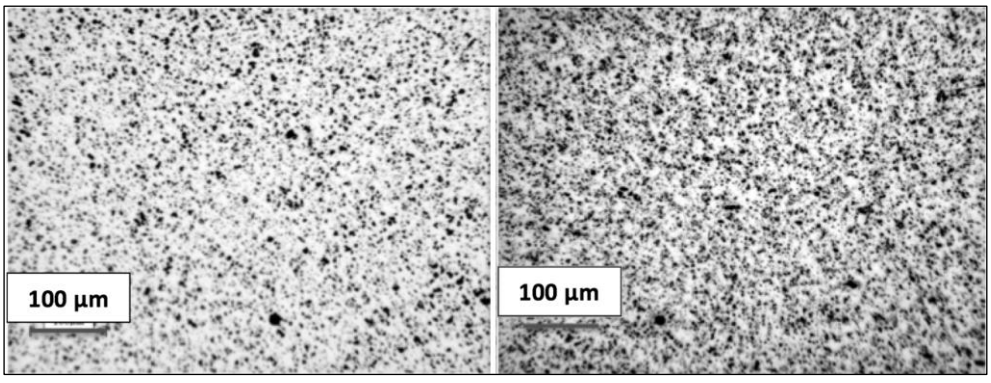

Figure 6: *200x light micrographs for sintered samples - (Left) HS; (Right) LTS B_4C*

Fig. 7 shows the SEM images gathered for the pressed and cut faces of all the pure, sintered B_4C samples. It can be seen that the samples exhibit an equiaxed, angular and fine grain structure. This corroborates SEM of commercial grade B_4C samples that have been consolidated in a similar manner in the literature [10–13].

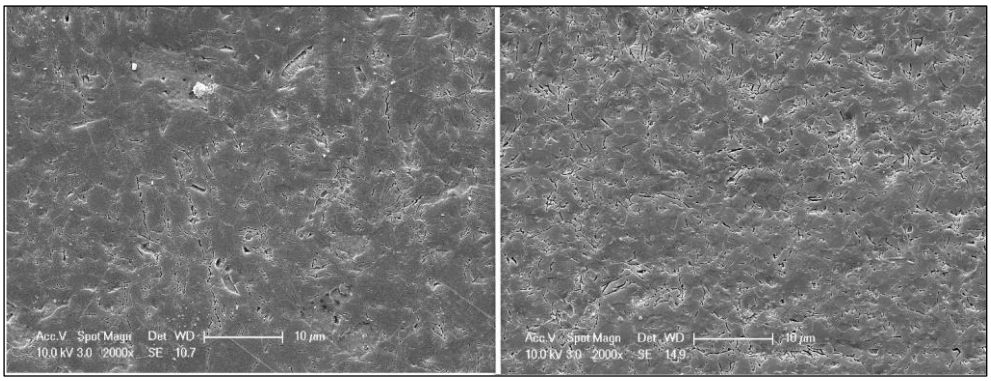

Figure 7: *2000x SE images for sintered samples – (left) HS; (right) LTS B_4C; 10 µm scale bar*

Fig. 8 shows the SEM micrographs for the fracture surfaces of the pure HS and LTS based samples. Both of these fracture surfaces are smooth and do not reveal much crack deflection, indicating transgranular fracture.

Figure 8: *2000x SE fracture surface images for sintered samples – (left): HS and (right): LTS B_4C – 20 µm scale bar*

Table 2 reveals that the matrix phases of both materials are made of B and C – indicating boron carbide. Small amounts of O indicate the presence of residual OPS silica particles used in the material polishing stages.

Table 2: *Average EDS atomic percentage compositions for sintered HS and LTS samples*

Sample/region	At.% B	At.% C	At.% O	At.% Si
HS - matrix	51.70	43.35	N/A	N/A
LTS - matrix	51.63	38.44	2.52	N/A

Table 3 compares the grain sizes of the sintered HS and LTS based samples using different measurement techniques. Of all the methods used, it is assumed Feret geometry is the most reliable since it takes the irregularity of the grains shape along 2 perpendicular axes into account. For the same reason, assuming spherical grain geometry is probably the least reliable method to evaluate each samples' grain size.

Table 3: *Average grain sizes of sintered samples using linear intercept and ImageJ*

Sample	Linear intercept / µm	ImageJ – spherical / µm	ImageJ – Feret / µm
HS	1.80 ± 0.39	1.67	1.35 ± 0.41
LTS	1.84 ± 0.07	1.72	1.26 ± 0.41

Table 3 shows that the average grain size values of LTS based samples using any specific method were greater on average than those gathered for the HS based samples. This corroborates the LSPS and SEM evidence in figs. 2 & 3 that suggests the as-synthesised LTS particles were coarser on average than the HS powder.

3.2.2. Raman Spectroscopy Studies on Sintered Samples

The Raman spectral peaks for the bright matrix phase of the sintered B_4C samples can be seen in fig 9. Features such as the peak doublet at 481 cm^{-1} and 531 cm^{-1} correlating to the inter icosahedral C-B-C bond stretching mode show that the HS and LTS samples maintained their B_4C stoichiometry after sintering [36–38].

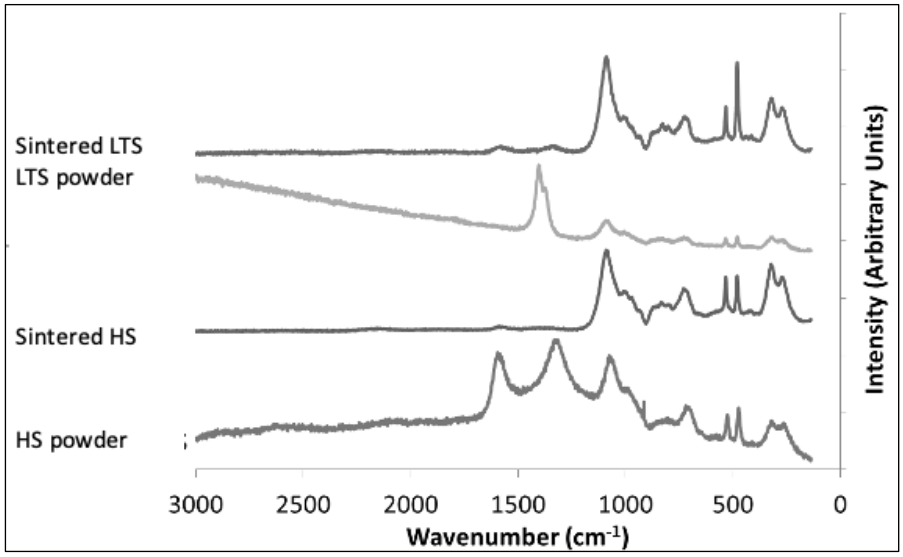

Figure 9: *Raman spectral peaks for HS and LTS B_4C before and after sintering*

3.2.3. XRD Studies on Powder Samples

Table 4 shows the results for the elemental and phase quantitative analysis for the B_4C samples. It shows that the total weight percentage of C in the HS grade B_4C is 22.4 wt.% C and 21.3 wt.% C for the LTS material. The value of the latter can be further decreased by carrying out the carbothermal reduction reaction under vacuum, which previous studies have shown to result in a C content of 20.6 wt.% C.

Table 4: *Weight percentages of phases present in powder samples*

Material	Total Weight Percentage of C – EA / wt.%	Free C Content – PQA / wt.%
HS powder	22.4	1.47
Sintered HS		0.94
LTS powder	21.3	0.61
Sintered LTS		0.17

Table 4 also suggests that this difference manifests itself as a lower residual C content, as opposed to a more B rich boron carbide polytype. It shows that the carbon contents were 1.47 and 0.94 wt.% C for the HS-based powder and sintered samples respectively. Both results corroborate those found in the literature for other commercial B_4C powders, which vary from 0.5-4.5 wt.% C [39–43]. The LTS samples, by contrast, contain 0.61 and 0.17 wt.% C in the powdered and sintered form respectively. These values rival those of other low-carbon B_4C powders made via alternative means, such as RCR, which vary between 0.1 – 1.3 wt.% C [43].

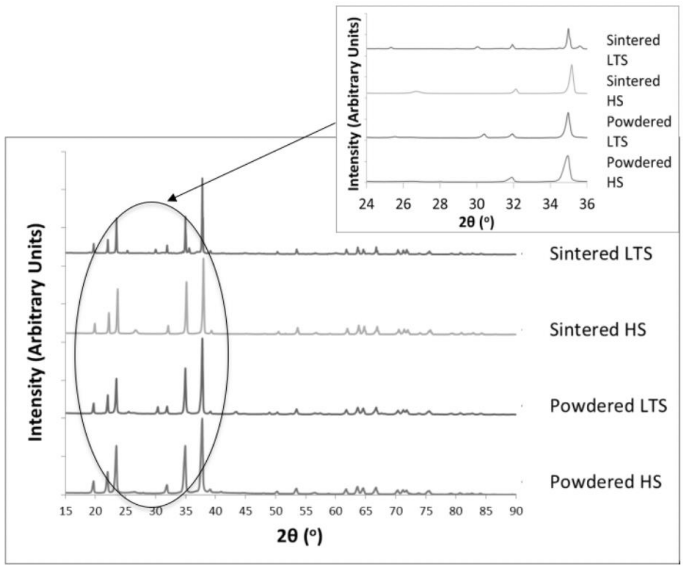

Figure 10: *XRD patterns of pre and post sintered HS and LTS B_4C (main: 15-90°, inset: 24-36° angle range)*

Fig. 10 shows the XRD patterns for the HS and LTS based samples. The 2 materials share the same main peak positions, which correspond to a B_4C structure. However, the peak at 26° corresponding to graphite is less acute in the LTS powder, thereby indicating that there is less present than in the HS powder. The former, by contrast, exhibits a peak at 30.4°. This corresponds to zirconia (ZrO_2), which is likely to exist as a micronising contaminant alongside Al_2O_3.

After sintering, 3 extra peaks arose in the LTS material. The peak at 20° most closely corresponds to B_4C, whereas peaks at 25.1° & 34.9° indicate the presence of ZrO_2 and aluminium diboride (AlB_2) respectively. These could arise due to the migration and nucleation of ZrO_2, as well as the reaction of Al_2O_3 with the B_4C to form AlB_2 in sintering. PQA analysis predicts that <1 wt.% of ZrO_2, ZrB_2, AlB_2 and Al_2O_3 are present within the material.

3.2.4. Mechanical Properties of Sintered Samples

Table 5 lists the average mechanical properties of the sintered HS grade B_4C relative to its LTS based counterpart. It can be seen that the pure LTS material is harder than the sintered HS grade material. The samples made with the HS grade powders exhibited similar results to those of Liu et al [44] and Tan et al [45], who made samples with Vickers hardness values of 28.8 GPa and 37.6 GPa respectively.

Table 5: *Mechanical properties of sintered B_4C samples*

Material	Parallel to Press Axis / GPa	Perpendicular to Press Axis / GPa	E / GPa	CPR / $MPam^{0.5}$
HS	32.5 (± 1.0)	31.4 (±1.9)	394.77 (±17.33)	4.43 (±0.78)
LTS	37.8 (±1.7)	35.8 (±1.6)	387.21 (±15.28)	3.34 (± 0.56)

Despite the fact that the average Young's Modulus and CPR values of the HS samples (394.77 GPa and 4.43 $MPam^{0.5}$) are higher than the LTS grade samples (387.21 GPa and 3.34 $MPam^{0.5}$), the standard deviations of these values overlap. This signifies that these values are similar to each other in these materials. Liu et al. [44] obtained similar values and error margins to those found in this study. Fig. 11 shows the SEM images of the Vickers indents in the sintered HS and LTS samples. None of the samples display radial crack deflection behaviour. These results are similar to those found when carrying out such tests on similar materials in the literature [44–48].

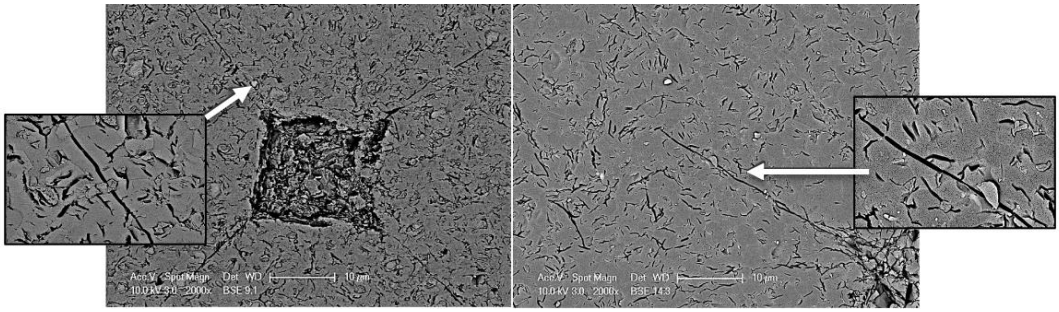

Figure 11: *2000x radial crack micrographs – (Left): HS; (Right): LTS; 10 µm scale bar*

4. Conclusions

This study has shown that it is possible to make B_4C using the LTS method. These powders exhibited a high chemical purity, as well as a lower total (21.3 wt.% C) and residual carbon content (1.47 and 0.94 wt.% C before and after sintering) than their commercially available counterparts (22.4 wt.% C, 0.61 and 0.17 wt.% C before and after sintering). Since graphite has a lower hardness (0.62-0.87 GPa) than B_4C, the average hardness of the sintered LTS samples (37.8 GPa) was higher than their HS counterparts (32.5 GPa), which is beneficial in applications requiring high hardness.

This study has also shown that drying the as-received LTS precursor material, followed by de-agglomerating it before and after pyrolysis, as well as after carbothermal reduction, yielded a higher proportion of primary ceramic particles, thereby lowering the powders' average grain size. Nevertheless, the particle size of the LTS B_4C (10.8 μm) was still far coarser than its commercial grade counterpart (2.4 μm), making the former more difficult to sinter.

5. Acknowledgements

The authors would like to thank Professor Peter M. Brown (formerly DSTL) and François Barthelemy (DGA) for the project funding through the UK-France PhD scheme (grant no: DSTLX- 1000092033).

6. Appendix

The following collection codes were used from the Crystal Structure Database for XRD analysis of the samples: B_4C (62713), $B_{13}C_2$ (8030), graphite (76767), B_2O_3 (16021), Al_2O_3 (9770), ZrO_2 (18190), AlB_2 (52282) and ZrB_2 (30327) [23].

7. References

1. Hazell PJ. Ceramic armour : design, and defeat mechanisms. Argos Press; 2006. 168 p.
2. Hazell PJ. Armour : materials, theory, and design. 1st ed. Press C, editor. Boca Raton, Florida: Taylor & Francis Group; 2016.
3. Chen M, McCauley JW, Hemker KJ. Shock-induced localized amorphization in boron carbide. Science. 2003 Mar 7;299(5612):1563–6.
4. Roberson C. Ballistic Testing of Boron Carbide Samples : Setting a Performance Baseline Comparator for the Assessment of Siliconized Boron Carbide Materials made under the Dstl funded SiBA research. 2016;
5. Subhash G, Awasthi AP, Kunka C, Jannotti P, DeVries M. In search of amorphization-resistant boron carbide. Scr Mater. 2016;123:158–62.
6. Perevislov SN, Lysenkov AS, Vikhman S V. Effect of Si additions on the microstructure and mechanical properties of hot-pressed B4C. Inorg Mater. 2017 Apr 1;53(4):376–80.
7. Proctor JE, Bhakhri V, Hao R, Prior TJ, Scheler T, Gregoryanz E, et al. Stabilization of boron carbide via silicon doping. J Phys Condens Matter. 2014 Jan 14;27(1):015401.

8. Mondal S, Bykova E, Dey S, Ali SI, Dubrovinskaia N, Dubrovinsky L, et al. Disorder and defects are not intrinsic to boron carbide. Sci Rep. 2016 Jan 18;6:19330.
9. Chuvashova I, Bykova E, Bykov M, Svitlyk V, Dubrovinsky L, Dubrovinskaia N. Structural stability and mechanism of compression of stoichiometric B13C2 up to 68GPa. Sci Rep. 2017 Aug 21;7(1):8969.
10. Hayun S, Paris V, Dariel MP, Frage N, Zaretzky E. Static and dynamic mechanical properties of boron carbide processed by spark plasma sintering. J Eur Ceram Soc. 2009;29(16):3395–400.
11. Kim KH, Chae JH, Park JS, Ahn JP, Shim KB. Sintering Behaviour and Mechanical Properties of B4C Ceramics Fabricated by Spark Plasma Sintering. J Ceram Process Res. 2009;10(6):716–20.
12. Li X, Jiang D, Zhang J, Lin Q, Chen Z, Huang Z. Densification behavior and related phenomena of spark plasma sintered boron carbide. Ceram Int. 2014;40(3):4359–66.
13. Sairam K, Sonber JK, Murthy TSRC, Subramanian C, Fotedar RK, Nanekar P, et al. Influence of spark plasma sintering parameters on densification and mechanical properties of boron carbide. Int Hournal Refract Met Hard Mater. 2014;42:185–92.
14. Mondal S, Banthia AK. Low-temperature synthetic route for boron carbide. J Eur Ceram Soc. 2005;25(2-3 SPEC. ISS.):287–91.
15. Hadian AM, Bigdeloo JA, Hadian AM, Bigdeloo JA. The Effect of Time , Temperature and Composition on Boron Carbide Synthesis by Sol-gel Method. J Mater Eng Perform. 2008;17(February):44–9.
16. Weimer AW, Roach RP, Haney CN, Moore WG, Rafaniello W. Rapid carbothermal reduction of boron oxide in a graphite transport reactor. AIChE J. 1991 May 1;37(5):759–68.
17. Toksoy MF, Rafaniello W, Xie KY, Ma L, Hemker KJ, Haber RA. Densification and characterization of rapid carbothermal synthesized boron carbide. Int J Appl Ceram Technol. 2017 May 1;14(3):443–53.
18. Munir Z a., Anselmi-Tamburini U, Ohyanagi M. The effect of electric field and pressure on the synthesis and consolidation of materials: A review of the spark plasma sintering method. J Mater Sci [Internet]. 2006 Feb;41(3):763–77. Available from: http://link.springer.com/10.1007/s10853-006-6555-2
19. Munir Z a., Anselmi-Tamburini U, Ohyanagi M. The effect of electric field and pressure on the synthesis and consolidation of materials: A review of the spark plasma sintering method. J Mater Sci. 2006 Feb;41(3):763–77.
20. Sevim F, Demir F, Bilen M, Okur H. Kinetic analysis of thermal decomposition of boric acid from thermogravimetric data. Korean J Chem Eng [Internet]. 2006 Sep [cited 2018 Jul 11];23(5):736–40. Available from: http://link.springer.com/10.1007/BF02705920
21. Gao L. Low Temperature Synthesis of Boron Carbide Powder for Body Armour Application. Birmingham; 2013.
22. Herth S, Joost WJ, Doremus RH, Siegel RW. New Approach to the Synthesis of Nanocrystalline Boron Carbide. J Nanosci Nanotechnol. 2006 Apr 1;6(4):954–9.
23. Physical Sciences Data-Science Service. Crystal Structure Database. 2017. Available from: https://www.psds.ac.uk/

24. ASTM International. E112: Standard Test Methods for Determining Average Grain Size. Astm E112-13 [Internet]. 1996 [cited 2018 Jul 11];1–28. Available from: https://compass.astm.org/download/E112.19798.pdf
25. ANSTIS GR, CHANTIKUL P, LAWN BR, MARSHALL DB. A Critical Evaluation of Indentation Techniques for Measuring Fracture Toughness: I, Direct Crack Measurements. J Am Ceram Soc [Internet]. 1981 Sep [cited 2018 Jul 11];64(9):533–8. Available from: http://doi.wiley.com/10.1111/j.1151-2916.1981.tb10320.x
26. Domnich V, Gogotsi Y, Trenary M, Tanaka T. Nanoindentation and Raman spectroscopy studies of boron carbide single crystals. Appl Phys Lett [Internet]. 2002 Nov 11 [cited 2018 Jul 9];81(20):3783–5. Available from: http://aip.scitation.org/doi/10.1063/1.1521580
27. Ge D, Domnich V, Juliano T, Stach E., Gogotsi Y. Structural damage in boron carbide under contact loading. Acta Mater [Internet]. 2004 Aug 2 [cited 2018 Jul 9];52(13):3921–7. Available from: https://www.sciencedirect.com/science/article/pii/S1359645404002691
28. Yan XQ, Li WJ, Goto T, Chen MW. Raman spectroscopy of pressure-induced amorphous boron carbide. Appl Phys Lett [Internet]. 2006 Mar 27 [cited 2018 Jul 9];88(13):131905. Available from: http://aip.scitation.org/doi/10.1063/1.2189826
29. Subhash G, Ghosh D, Blaber J, Zheng JQ, Halls V, Masters K. Characterization of the 3-D amorphized zone beneath a Vickers indentation in boron carbide using Raman spectroscopy. Acta Mater [Internet]. 2013 Jun 1 [cited 2018 Jul 9];61(10):3888–96. Available from: https://www.sciencedirect.com/science/article/pii/S1359645413002383
30. Parsard G, Subhash G. Raman spectroscopy mapping of amorphized zones beneath static and dynamic Vickers indentations on boron carbide. J Eur Ceram Soc. 2017;37(5):1945–53.
31. Ye F, Hou Z, Zhang H, Liu L. Densification and mechanical properties of spark plasma sintered B 4C with si as a sintering aid. J Am Ceram Soc. 2010 Oct 1;93(10):2956–9.
32. Sinha A, Mahata T, Sharma BP. Carbothermal route for preparation of boron carbide powder from boric acid-citric acid gel precursor. J Nucl Mater [Internet]. 2002 Mar 1 [cited 2018 Jul 12];301(2–3):165–9. Available from: https://www.sciencedirect.com/science/article/pii/S0022311502007043
33. Alizadeh a., Taheri-Nassaj E, Ehsani N. Synthesis of boron carbide powder by a carbothermic reduction method. J Eur Ceram Soc. 2004;24(10–11):3227–34.
34. Alizadeh A, Taheri-Nassaj E, Ehsani N, Baharvandi HR. Production of boron carbide powder by carbothermic reduction from boron oxide and petroleum coke or carbon active. Adv Appl Ceram [Internet]. 2006 Dec 18 [cited 2018 Jul 12];105(6):291–6. Available from: http://www.tandfonline.com/doi/full/10.1179/174367606X146685
35. Dacic BZ, Jokanovi V, Jokanovi B, Dramianin MD. Thermodynamics of gas phase carbothermic reduction of boron-anhydride. J Alloys Compd. 2006;413(1–2):198–205.
36. Tallant, D.R.; Aselage, T.L.; Campbell, A.N.; Emin D. Boron Carbide Structure by Raman Spectroscopy. Am Phys Soc. 1989;8(40):5649–56.

37. Lazzari R, Vast N, Besson JM, Baroni S, Dal Corso A. Atomic Structure and Vibrational Properties of Icosahedral B 4 C Boron Carbide. Phys Rev Lett [Internet]. 1999 Oct 18 [cited 2018 Jul 9];83(16):3230–3. Available from: https://link.aps.org/doi/10.1103/PhysRevLett.83.3230
38. Kunka C, Awasthi A, Subhash G. Crystallographic and spectral equivalence of boron-carbide polymorphs. Scr Mater. 2016;122:82–5.
39. Beauvy M, Angers R. METHOD FOR THE DETERMINATION OF FREE GRAPHITE IN BORON CARBIDE. J Less-Common Met. 1981;80(22):7–233.
40. McCuiston R, LaSalvia J, McCauley J, Mayo W. The Possible Roles of Stoichiometry, Microstructure, and Defects on the Mechanical Behavior of Boron Carbide. In: Advances in Ceramic Armor IV: Ceramic Engineering and Science Proceedings. John Wiley & Sons, Inc.; 2009. p. 153–62.
41. Kuwelkar K, Domnich V, Haber RA. Assessing the Carbon Concentration in Boron Carbide: A Combined X-Ray Diffraction and Chemical Analysis. In: Advances in Ceramic Armor X. John Wiley & Sons, Inc.; 2014. p. 103–9.
42. Bakhshi M, Arab H, Amini MK. Comparison of sample preparation methods for determination of free carbon in boron carbide by X-ray powder diffraction. J Iran Chem Soc [Internet]. 2016 Sep 10 [cited 2018 Jul 11];13(9):1673–81. Available from: http://link.springer.com/10.1007/s13738-016-0884-0
43. Gao Y, Etzold A, Munhollon T, Rafaniello W, Haber R. Processing factors influencing the free carbon contents in boron carbide powder by rapid carbothermal reduction. Diam Relat Mater. 2016;61:14–20.
44. Liu L, Wang Y, Li X, Xu L, Cao X, Wang Y, et al. Enhancing Toughness in Boron Carbide with Reduced Graphene Oxide. J Am Ceram Soc. 2016;99(1):257–64.
45. Tan Y, Zhang H, Peng S. Electrically conductive graphene nanoplatelet / boron carbide composites with high hardness and toughness. Scr Mater. 2016;114:98–102.
46. Yavas B, Sahin F, Yucel O, Goller G. Effect of particle size, heating rate and CNT addition on densification, microstructure and mechanical properties of B4C ceramics. Ceram Int. 2015;41(7):8936–44.
47. Kovalčíková a., Sedlák R, Rutkowski P, Dusza J. Mechanical properties of boron carbide+graphene platelet composites. Ceram Int. 2016;42(1):2094–8.
48. Sedlák R, Kovalčíková A, Múdra E, Rutkowski P, Dubiel A, Girman V, et al. Boron carbide/graphene platelet ceramics with improved fracture toughness and electrical conductivity. J Eur Ceram Soc. 2017;37(12):3773–80.